High-Resolution VUV Spectra of Carbon, Neon and Argon in a Wavelength Range of 250 to 2300 Å for Plasma Diagnostics Observed with a 3 m Normal Incidence Spectrometer in LHD

Ryuji KATAI, Shigeru MORITA[1)] and Motoshi GOTO[1)]

Department of Fusion Science, The Graduate University for Advanced Studies, Toki 509-5292, Japan
[1)]*National Institute for Fusion Science, Toki 509-5292, Japan*

Intrinsic impurities have been much reduced in toroidal fusion devices through the development of several wall-conditioning techniques as well as by the use of carbon materials in the first wall and divertor plates. Impurity elements useful for passive plasma spectroscopy have been then extremely limited. At present, only carbon is a subject for spectroscopic diagnostics in most discharges except for fuel atoms. The use of rare gas as a brighter light source is a method to overcome the present difficulty in passive spectroscopy. Recently, rare gases have also been used for edge cooling to reduce the divertor heat flux. Therefore, high-resolution spectra ($\Delta\lambda \sim 0.2$ Å) from neon and argon in a 250 to 2300 Å wavelength range have been measured using a 3 m normal incidence spectrometer in Large Helical Device (LHD) and the measured spectra were precisely analyzed. The VUV spectra of carbon, neon and argon are presented for spectroscopic use and their wavelengths are tabulated with their relative intensities. The spectral profiles of almost all the spectral lines measured here are formed by the Doppler broadening and self-absorption processes. The Doppler broadening of neon and argon spectra are plotted against the ionization energies and Doppler spectra from carbon lines are presented. The self-absorption spectra of the hydrogen Lyman-α line, which are found in the LHD high-density discharge, are also presented and the neutral density is analytically estimated.

1. Introduction

The purpose of passive plasma spectroscopy in fusion research is mainly to diagnose the particle behaviors of impurity and fuel atoms and ions, including the measurement of line radiation loss in addition to the contribution to atomic physics [1]. The resonance lines from highly ionized impurities are emitted in vacuum ultraviolet (VUV) region. For this purpose, usually the first resonance lines have been measured though visible lines are useful for divertor spectroscopy. Therefore, VUV spectroscopy becomes important for passive plasma spectroscopy and the resonance lines from typical intrinsic impurities such as carbon, oxygen and iron have been routinely measured in the VUV region in many magnetic fusion devices [2–11].

On the other hand, several wall-conditioning techniques have been recently progressed. These include high-temperature baking of plasma facing components, He-glow discharge for wall cleaning and boronization of the vacuum wall. In addition, the vacuum wall has been fully covered by carbon plates and such plates have been also installed in the divertor section. Thus, the impurity concentrations in toroidal fusion devices have been much re-duced. Due to advances in wall-conditioning, spectral lines useful for passive spectroscopy in VUV region have been very limited except in regard to the carbon emissions. External impurity injection is needed for the study of impurity behaviors. The use of rare gas is an effective method to overcome the present difficult situation in the passive spectroscopy. At present, neon or argon is a possible candidate for the seeded gas. In ITER, the use of krypton is planned for use in spectroscopic diagnostics. Recently, such rare gases have been also used for edge plasma cooling based on the enhancement of radiation loss in order to reduce the divertor heat flux [12]. Therefore, it becomes important to investigate and identify the VUV spectral lines emitted from highly ionized ions of such rare gas elements for alternative spectroscopic measurement in fusion devices.

Large Helical Device (LHD) is a toroidal plasma device without plasma current for confinement. Rare gas discharges are easily produced in LHD because current-driven MHD instability can be essentially avoided. The upper limit of densities in such high-Z discharges in LHD is determined by measuring the radiation loss at outer region of the plasma depending on the input heating power, i.e., typically 2×10^{19} m^{-3} for Ar discharges at $P_{\mathrm{NBI}} \sim 10$ MW and $B_{\mathrm{t}} = 2.75$ T. This is far from the beta collapse value. Thus,

the VUV spectra of highly ionized rare gases such as neon and argon are studied using the rare gas discharges in LHD. The central electron density and temperature of the rare gas discharges used for the present study are in the ranges of 10^{18}-10^{19} m^{-3} and 2-4 keV, respectively. The VUV spectra in a wavelength of 250 to 2300 Å are observed using a 3 m normal incidence spectrometer with a high spectral resolution of $\Delta\lambda \sim 0.2$ Å. The spectral resolution observed here is narrower than the Doppler broadening of most of the VUV lines emitted from the LHD plasmas. Therefore, the VUV spectra measured here can give the highest level of spectral resolution as compared with the former results. In this paper, the VUV spectra from carbon, neon and argon are presented and the wavelengths are tabulated with their relative intensities, the full width at half maximum (FWHM) and the ion temperature for spectroscopic use. Typical spectral lines useful for spectroscopic diagnostics of high-temperature plasmas are also summarized for the three elements. A self-absorption spectrum is observed in the Lyman series of neutral hydrogen instead of the Doppler broadening. The spectra of the hydrogen Lyman series are also presented with an analysis.

2. Instrumentation

VUV spectra have been measured using a space-resolved VUV system, which consists of a 3 m normal incidence spectrometer with a 1200 grooves/mm grating (65×150 mm^2, 1400 Å blaze with Pt coating), a back-illuminated charged-coupled device (CCD) detector (1024×1024 pixels, 13 μm $\times$ 13 μm/pixel) and a pair of mirrors for view-angle adjustment [13–15]. The size of the CCD exposure area is 13.3×13.3 mm^2. The spectrometer has a reciprocal linear dispersion of 2.75 Å/mm (0.036 Å/ch) and a spectral resolution of $\Delta\lambda \sim 0.2$ Å at FWHM which is constant against the wavelength. The total spectral resolution corresponds to the CCD channel width of 5.6 pixels which is determined by the spectral resolution of the 3 m normal incidence spectrometer. The view-angle mirrors mounted in front of an entrance slit of the spectrometer were removed and a space-resolved slit positioned between the entrance slit and the grating was fully opened for recording sufficient signal counts with an adequate S/N ratio. The entrance slit was set to a width of 20 μm. The CCD detector was cooled to -20°C in order to reduce thermal noise. The noise count was less than 1 count/pixel at this temperature. The CCD detector was operated in 'full-binning mode', which performs a full summation of vertical pixels, in order to increase the signal counts and to reduce the exposure time (or frame rate). The time interval of the CCD frame exposure was set to 50 ms, which was adequate for taking the spectra with a sufficient S/N ratio. The spectral range of 38 Å was measured in a single discharge. Therefore, in the present study the wavelength of the spectrometer was scanned in shot by shot in order to observe the entire spectral range.

3. Results and Discussion
3.1 Line identification of C, Ne and Ar

Identification of the VUV spectrum was compiled by using previously reported experimental spectra and wavelength tables [16–24]. The VUV spectra were obtained by scanning the wavelength of the spectrometer shot by shot. Figures 1 (a) to 1 (g) show VUV spectra from neon discharges in the wavelength range of 250 to 1275 Å. A VUV spectrum of 2257-2296 Å is shown in bottom trace of Fig. 1 (g) with He-like CV (ionization potential: 392 eV) line at 2270 Å. Below 435 Å, VUV spectra having relatively strong emissions from metallic impurities of iron and chromium ions (Na- and Mg-like) are specially selected as an exception of the present work. This will be useful as a reference for spectroscopic use.

Figures 2 (a) to 2 (i) show VUV spectra from argon discharges in the wavelength range of 355 to 1565 Å. In Figs. 2 (a) to 2 (i), oxygen and nitrogen lines appear with relatively strong intensities, because the data are taken just after a small amount of air leaked into the vacuum vessel. This is a useful reference for diagnostics of light impurities. A small amount of boron is also seen in the spectra. Boronization is carried out to create a boron coating on the stainless steel vacuum wall in order to suppress the metallic impurities.

Carbon lines identified from the spectra are listed in Table 1. The order in the table denotes the maximum number of higher order lines seen in the figures. The relative
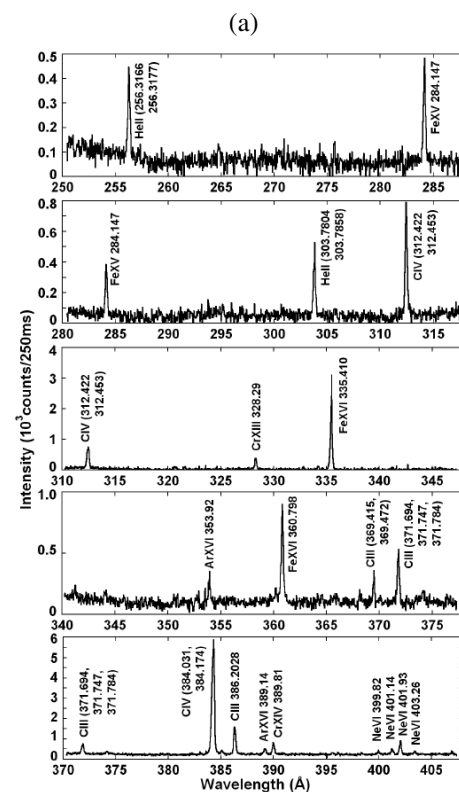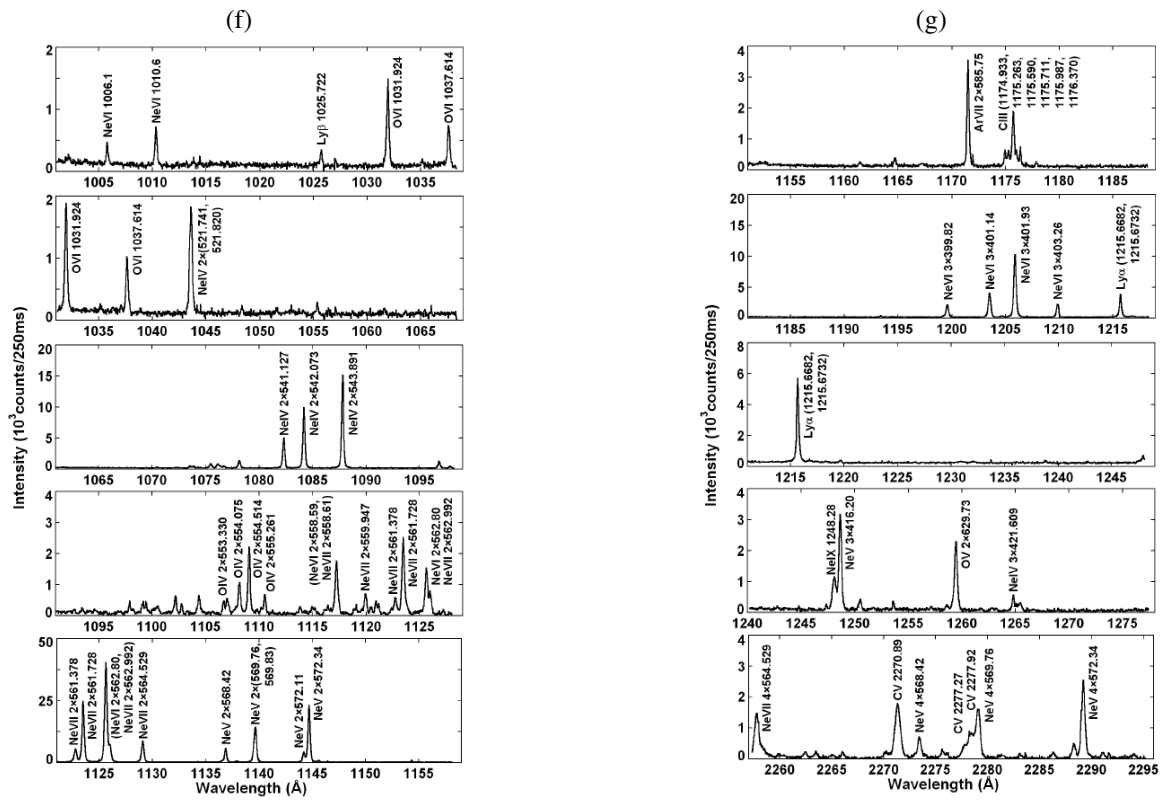
(a)

Fig. 1   VUV spectra from neon discharges.

Fig. 1 (*continued*)

(f)

(g)

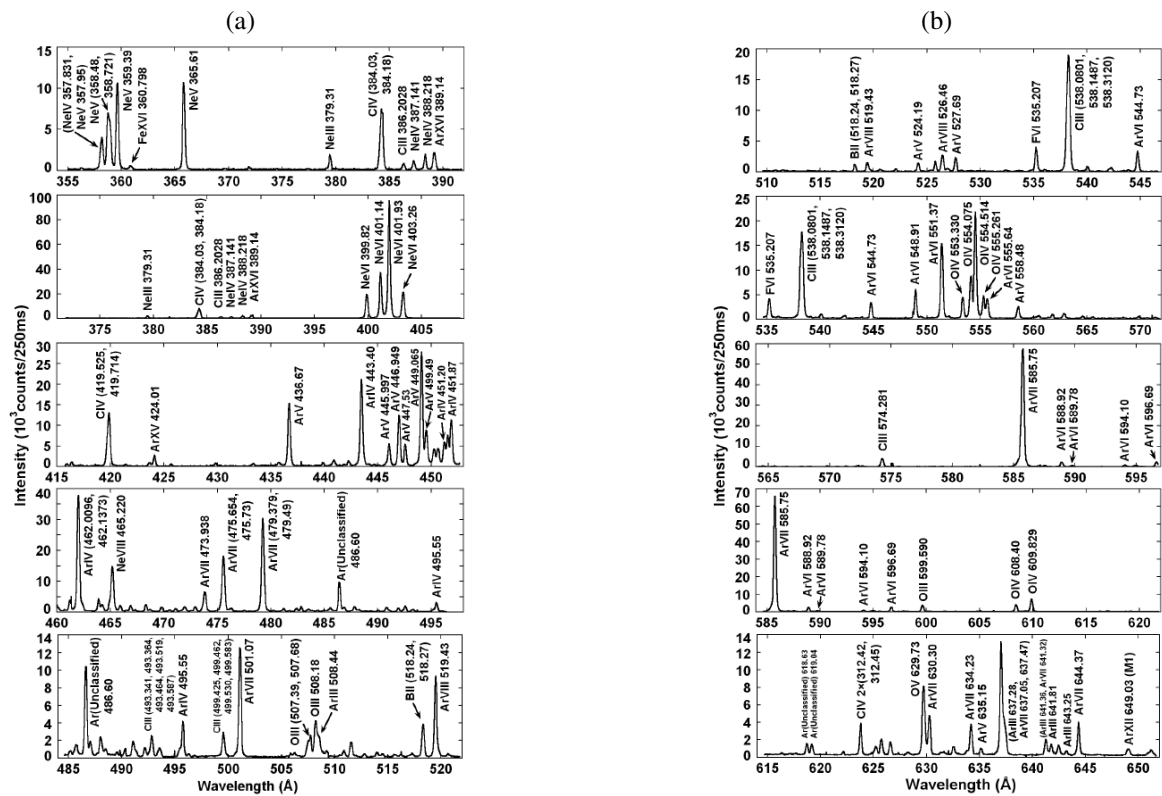Fig. 1   (*continued*)

(a)

(b)

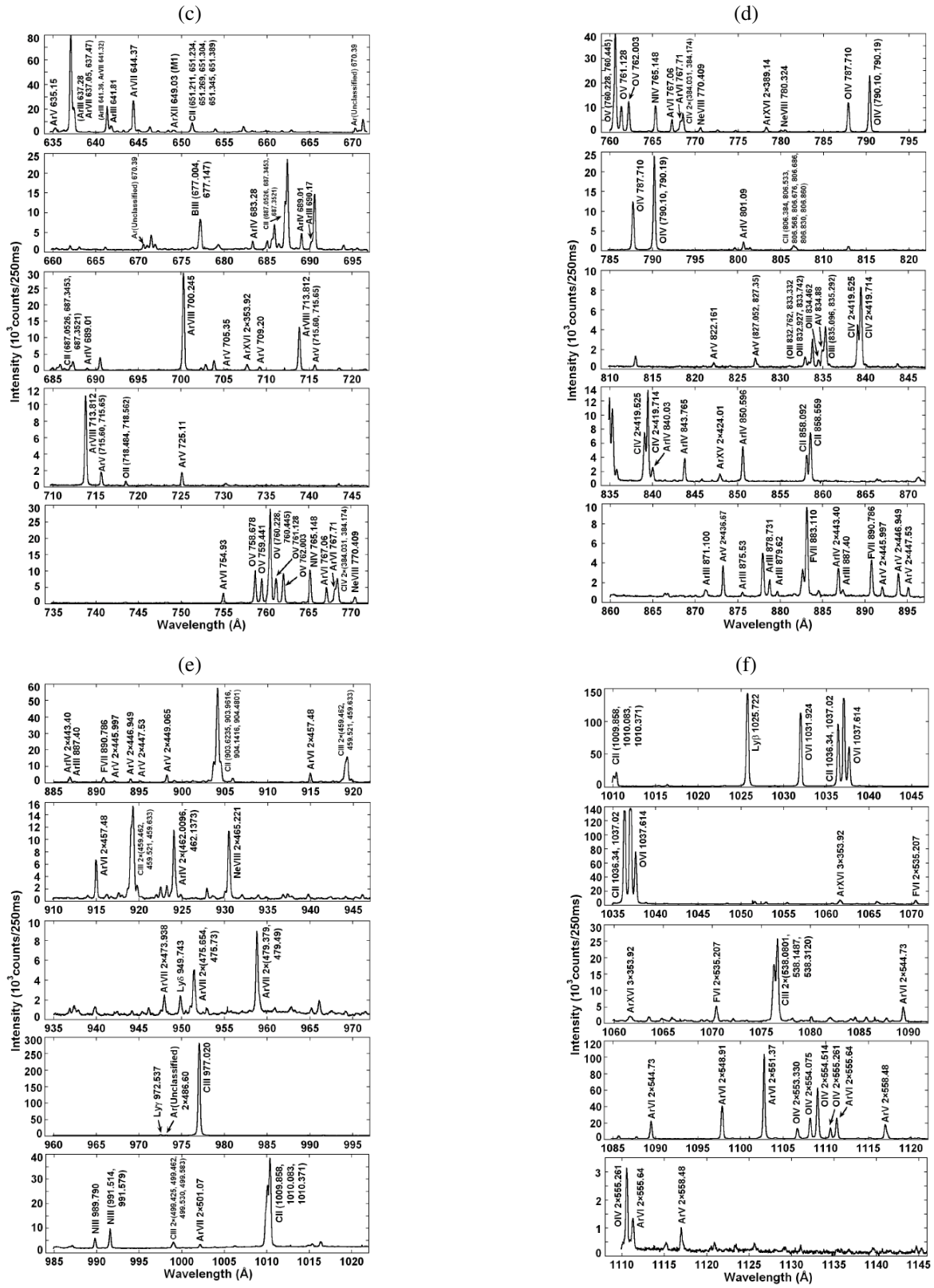Fig. 2   VUV spectra from argon discharges.
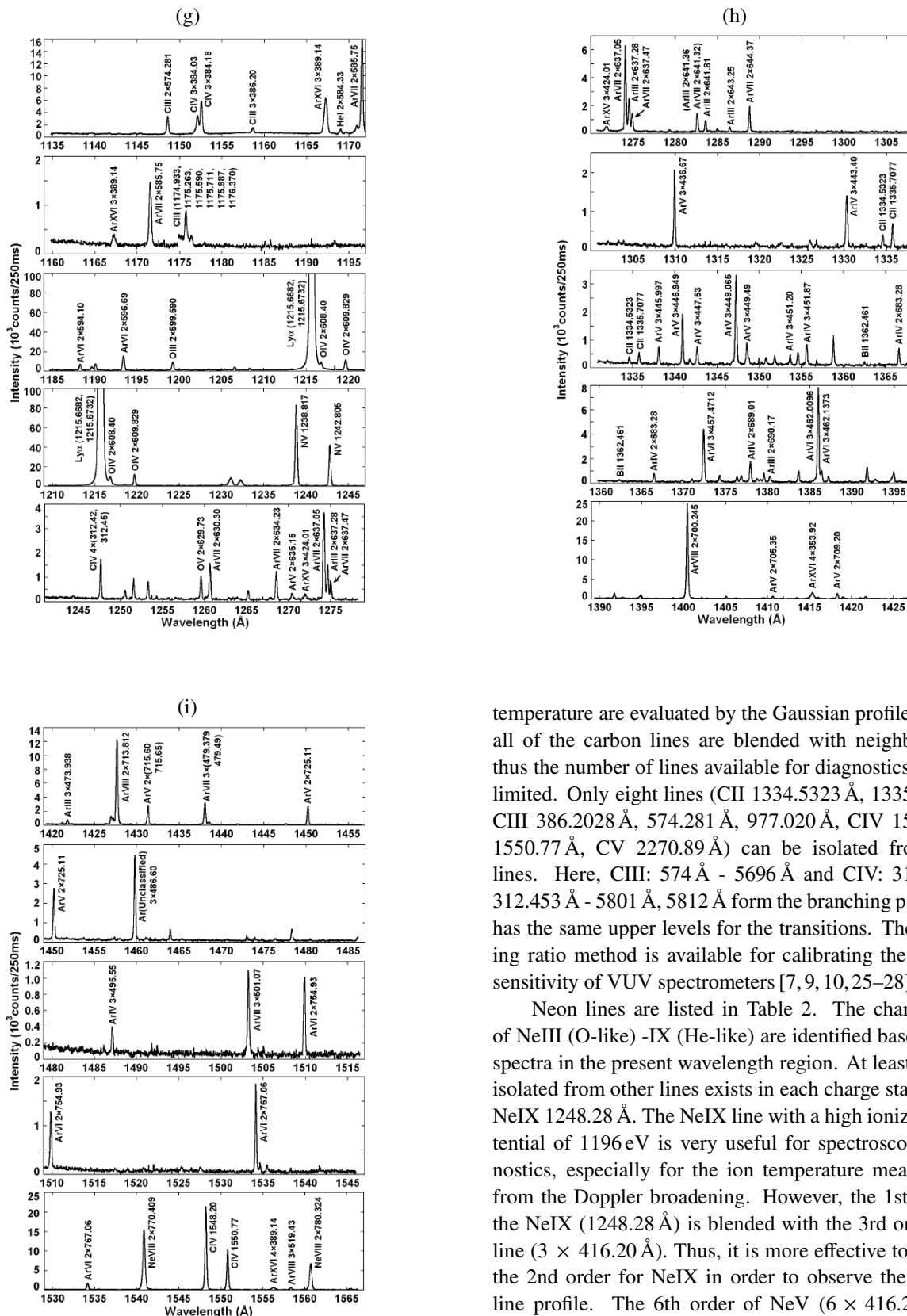
Fig. 2   (*continued*)

Fig. 2 (*continued*)

intensity is defined by total counts summed over the line spectral range based on a least-square Gaussian fitting of the measured spectral profile, and the FWHM and the ion temperature are evaluated by the Gaussian profile. Almost all of the carbon lines are blended with neighbor lines, thus the number of lines available for diagnostics are very limited. Only eight lines (CII 1334.5323 Å, 1335.7077 Å, CIII 386.2028 Å, 574.281 Å, 977.020 Å, CIV 1548.20 Å, 1550.77 Å, CV 2270.89 Å) can be isolated from other lines. Here, CIII: 574 Å - 5696 Å and CIV: 312.422 Å, 312.453 Å - 5801 Å, 5812 Å form the branching pair which has the same upper levels for the transitions. The branching ratio method is available for calibrating the absolute sensitivity of VUV spectrometers [7, 9, 10, 25–28].

Neon lines are listed in Table 2. The charge states of NeIII (O-like) -IX (He-like) are identified based on the spectra in the present wavelength region. At least one line isolated from other lines exists in each charge state except NeIX 1248.28 Å. The NeIX line with a high ionization potential of 1196 eV is very useful for spectroscopic diagnostics, especially for the ion temperature measurement from the Doppler broadening. However, the 1st order of the NeIX (1248.28 Å) is blended with the 3rd order NeV line (3 × 416.20 Å). Thus, it is more effective to measure the 2nd order for NeIX in order to observe the accurate line profile. The 6th order of NeV (6 × 416.20 Å) becomes much weaker as compared to the 2nd order of NeIX (2 × 1248.28 Å) and the separation between the two lines is also clearer in case of the 2nd order for NeIX.

Argon lines are listed in Table 3. In the case of argon, the magnetic dipole (M1) transition (ArXII 649.03 Å) is observed [29–31]. This is the first observation in laboratory plasmas. In tokamaks the maintenance of high-*Z* dis-

Table 1 Wavelength list of carbon lines. Symbol of 'b' in relative intensity means the line is blended with other lines.

Wavelength (Å)	Ion charge state	Order	Relative intensity	FWHM (pixels)	FWHM (Å)	Ion temperature (eV)
312.422	CIV	2	b			
312.453	CIV	2	b			
319.415	CIII	1	b			
369.472	CIII	1	b			
371.694	CIII	1	b			
371.747	CIII	1	b			
371.784	CIII	1	b			
384.031	CIV	3	b			
384.174	CIV	3	b			
386.2028	CIII	3	4.4	5.1	0.18	< 5
419.525	CIV	2	b			
419.714	CIV	2	b			
459.462	CIII	2	b			
459.521	CIII	2	b			
459.633	CIII	2	b			
493.341	CIII	1	b			
493.364	CIII	1	b			
493.396	CIII	1	b			
493.464	CIII	1	b			
493.519	CIII	1	b			
493.587	CIII	1	b			
499.425	CIII	2	b			
499.462	CIII	2	b			
499.53	CIII	2	b			
499.583	CIII	2	b			
538.08	CIII	2	b			
538.1487	CIII	2	b			
538.312	CIII	2	b			
574.281	CIII	2	27.5	4.7	0.17	< 5
641.593	CII	1	b			
641.627	CII	1	b			
641.771	CII	1	b			
641.8	CII	1	b			
641.888	CII	1	b			
651.211	CII	1	b			
651.234	CII	1	b			
651.269	CII	1	b			
651.304	CII	1	b			
651.345	CII	1	b			
651.389	CII	1	b			
687.0526	CII	1	b			
687.3453	CII	1	b			
687.3521	CII	1	b			
806.384	CII	1	b			
806.533	CII	1	b			
806.568	CII	1	b			
806.676	CII	1	b			
806.686	CII	1	b			
806.83	CII	1	b			
806.86	CII	1	b			
858.092	CII	1	b			
858.559	CII	1	b			
903.6235	CII	1	b			
903.9616	CII	1	b			
904.1416	CII	1	b			
904.4801	CII	1	b			
977.02	CIII	1	2429.6	5.7	0.21	< 5
1009.858	CII	1	b			
1010.083	CII	1	b			
1010.371	CII	1	b			
1036.34	CII	1	b			
1037.02	CII	1	b			
1174.933	CIII	1	b			
1175.263	CIII	1	b			
1175.59	CIII	1	b			
1175.711	CIII	1	b			
1175.987	CIII	1	b			
1176.37	CIII	1	b			
1334.532	CII	1	1.6	5.1	0.18	< 5
1335.708	CII	1	3.5	5.4	0.19	< 5
1548.2	CIV	1	116.9	5.8	0.21	5 ± 5
1550.77	CIV	1	58.4	5.9	0.21	6 ± 5
2270.89	CV	1	27.4	15.7	0.56	106 ± 12
2277.27	CV	1	b			
2277.92	CV	1	b			

Table 2 Wavelength list of neon lines. Symbol of 'b' in relative intensity means the line is blended with other lines.

Wavelength (Å)	Ion charge state	Order	Relative intensity	FWHM (pixels)	FWHM (Å)	Ion temperature (eV)
357.831	NeIV	2	b			
357.95	NeV	2	b			
358.48	NeV	2	b			
358.721	NeIV	2	b			
359.39	NeV	2	44.0	6.2	0.22	39 ± 30
365.61	NeV	2	46.4	6.3	0.23	51 ± 34
379.31	NeIII	2	6.8	6.0	0.22	13 ± 13
387.141	NeIV	1	4.5	7.0	0.25	131 ± 102
388.218	NeIV	1	7.5	6.6	0.24	37 ± 37
399.82	NeVI	3	138.1	6.5	0.23	54 ± 22
401.14	NeVI	3	269.9	6.4	0.23	51 ± 21
401.93	NeVI	3	696.2	6.5	0.23	55 ± 21
403.26	NeVI	3	153.0	6.7	0.24	77 ± 26
416.20	NeV	3	0.7	6.3	0.23	33 ± 18
416.82	NeV	3	4.8	6.4	0.23	45 ± 23
421.609	NeIV	3	6.7	6.2	0.22	25 ± 15
433.176	NeVI	2	b			
433.24	NeIV	2	b			
435.649	NeVI	2	54.4	6.7	0.24	61 ± 21
451.843	NeVI	2	8.1	5.8	0.20	40 ± 40
452.745	NeVI	2	15.7	6.5	0.23	175 ± 77
454.072	NeVI	2	24.3	6.7	0.24	216 ± 80
465.221	NeVII	2	976.1	7.2	0.26	347 ± 93
469.773	NeIV	2	b			
469.82	NeIV	2	b			
469.866	NeIV	2	b			
469.921	NeIV	2	b			
480.41	NeV	2	20.3	6.3	0.23	103 ± 50
481.28	NeV	2	b			
481.36	NeV	2	b			
482.99	NeV	2	109.8	6.6	0.24	168 ± 75
488.10	NeIII	2	8.4	6.0	0.21	28 ± 27
488.87	NeIII	2	7.5	6.1	0.22	56 ± 47
489.5	NeIII	2	b			
489.64	NeIII	2	b			
490.31	NeIII	2	6.4	5.6	0.20	16 ± 16
491.05	NeIII	2	9.1	5.9	0.21	24 ± 24
521.741	NeIV	2	b			
521.820	NeIV	2	b			
541.127	NeIV	2	49.1	6.2	0.22	65 ± 36
542.073	NeIV	2	101.7	6.1	0.22	54 ± 32
543.891	NeIV	2	155.8	6.1	0.22	52 ± 36
558.59	NeVI	2	b			
558.61	NeVII	2	b			
559.947	NeVII	2	100.3	6.7	0.24	143 ± 74
561.378	NeVII	2	b			
561.728	NeVII	2	b			
562.80	NeVI	2	b			
562.992	NeVII	2	b			
564.529	NeVII	2	126.4	7.2	0.26	245 ± 66
568.42	NeV	2	73.9	6.4	0.23	90 ± 42
569.76	NeV	2	b			
569.83	NeV	2	b			
572.11	NeV	2	b			
572.34	NeV	2	b			
770.409	NeVIII	2	1021.6	7.0	0.25	112 ± 31
780.324	NeVIII	2	492.0	7.0	0.25	108 ± 30
895.18	NeVII	1	23.5	6.6	0.24	53 ± 19
1006.1	NeVI	1	2.0	6.0	0.22	8 ± 8
1010.6	NeVI	1	3.7	6.3	0.23	22 ± 16
1248.28	NeIX	1	12.5	21.6	0.78	283 ± 47

Table 3 Wavelength list of argon lines. Symbol of 'ArUn' in ion charge state means the unclassified line and the ion charge in brackets after the 'ArUn' indicates possible ionization stage evaluated from the ion temperature. Symbol of 'b' in relative intensity means the line is blended with other lines.

Wavelength (Å)	Ion charge state	Order	Relative intensity	FWHM (pixels)	FWHM (Å)	Ion temperature (eV)
353.92	ArXVI	4	1.3	9.0	0.32	637 ± 127
389.14	ArXVI	4	12.8	9.4	0.34	615 ± 114
424.01	ArXV	3	16.4	9.2	0.33	480 ± 119
436.67	ArV	3	96.0	6.7	0.24	119 ± 61
443.40	ArIV	3	135.1	7.3	0.26	210 ± 80
445.997	ArV	3	32.7	6.2	0.22	45 ± 37
446.949	ArV	3	b			
447.53	ArV	3	b			
449.065	ArV	3	b			
449.49	ArV	3	b			
451.20	ArIV	3	b			
451.87	ArIV	3	b			
457.48	ArVI	3	41.3	6.9	0.25	144 ± 64
462.0096	ArIV	3	b			
462.1373	ArIV	3	b			
473.938	ArVII	3	b			
475.654	ArVII	3	b			
475.73	ArVII	3	b			
479.379	ArVII	3	b			
479.49	ArVII	3	b			
486.60	ArUn (III)	3	56.3	6.2	0.22	40 ± 32
495.55	ArIV	3	16.7	6.6	0.24	53 ± 53
501.07	ArVII	3	74.0	7.0	0.25	138 ± 57
508.44	ArIII	1	b			
519.43	ArVIII	3	68.9	6.9	0.25	111 ± 50
524.19	ArV	1	b			
526.46	ArVIII	1	b			
527.69	ArV	1	15.7	6.5	0.23	60 ± 35
544.73	ArVI	2	23.9	6.9	0.25	150 ± 45
548.91	ArVI	2	41.2	6.9	0.25	93 ± 43
551.37	ArVI	2	108.1	6.9	0.25	97 ± 44
555.64	ArVI	2	b			
558.48	ArV	2	b			
585.75	ArVII	2	478.3	6.7	0.24	288 ± 141
588.92	ArVI	1	16.5	6.5	0.24	214 ± 121
589.78	ArVI	1	3.7	6.5	0.24	218 ± 122
594.10	ArVI	2	6.2	6.7	0.24	258 ± 132
596.69	ArVI	2	18.6	6.6	0.24	240 ± 217
618.63	ArUn (VI-VIII)	1	8.4	6.5	0.23	194 ± 110
619.04	ArUn (VI-VIII)	1	8.2	6.7	0.24	248 ± 124
630.30	ArVII	2	b			
634.23	ArVII	2	23.4	6.6	0.24	217 ± 113
635.15	ArV	2	5.0	6.9	0.25	293 ± 131
637.05	ArVII	2	b			
637.28	ArIII	2	b			
637.47	ArVII	2	b			
641.36	ArIII	2	b			
641.32	ArVII	2	b			
641.81	ArIII	2	b			
643.25	ArIII	2	b			
644.37	ArVII	2	28.1	6.9	0.24	271 ± 158
649.03	ArXII	1	7.3	9.5	0.34	1136 ± 253
670.39	ArUn	1	b			
683.28	ArIV	2	14.8	6.5	0.23	159 ± 90
689.01	ArIV	2	27.2	6.5	0.23	141 ± 84
690.17	ArIII	2	b			
700.245	ArVIII	2	211.7	6.7	0.24	190 ± 96
705.35	ArV	2	0.8	5.4	0.19	< 50
709.20	ArV	2	7.3	6.8	0.25	220 ± 102
713.812	ArVIII	2	94.9	6.9	0.25	221 ± 101
715.60	ArV	2	b			
715.65	ArV	2	b			
725.11	ArV	2	11.1	6.5	0.23	134 ± 78
754.93	ArVI	2	21.5	6.6	0.24	153 ± 80
767.06	ArVI	2	34.1	6.8	0.25	184 ± 78
767.71	ArVI	1	b			
801.09	ArIV	1	15.0	7.0	0.25	194 ± 85
822.161	ArV	1	2.9	6.9	0.25	172 ± 78
827.052	ArV	1	b			
827.35	ArV	1	b			
834.88	ArV	1	b			
840.03	ArIV	1	b			
843.765	ArIV	1	22.9	6.7	0.24	125 ± 65
850.596	ArIV	1	35.6	6.7	0.24	134 ± 66
871.100	ArIII	1	b			
875.530	ArIII	1	2.6	6.3	0.23	70 ± 47
878.731	ArIII	1	11.4	6.6	0.24	108 ± 58
879.62	ArIII	1	3.1	6.4	0.23	81 ± 50
887.40	ArIII	1	b			

Table 4 Line lists of carbon, neon and argon VUV lines useful for spectroscopic measurement.

Ion charge state	Ionization potential (eV)	Wavelength (Å)
CII	24	1334.5323, 1335.7077
CIII	48	977.02
CIV	65	1548.20, 1550.77
CV	392	2270.89
NeIII	63	379.31
NeIV	97	421.609
NeV	126	365.61
NeVI	158	435.649
NeVII	207	465.221
NeVIII	239	770.409, 780.324
NeIX	1196	1248.28
ArIII	41	878.731
ArIV	60	443.4
ArV	75	436.67
ArVI	91	551.37
ArVII	124	585.75
ArVIII	143	700.245, 713.812
ArXV	854	424.01
ArXVI	918	353.92, 389.14

charges is generally difficult because of the current-driven instability, as mentioned above. This is a great benefit of LHD. As the ArXII M1 line is much weaker than resonance lines and the brightness of the VUV diagnostic system is darker than that of the visible diagnostic system, it was usually difficult to observe such Ar M1 line. In contrast, the maintenance of high-Z discharges is quite easy in LHD. Therefore, pure Ar discharges can be performed at an electron density region of $0.5\text{-}3 \times 10^{13}\,\text{cm}^{-3}$. This is the reason why the ArXII M1 line was found for the first time in LHD. Several M1 transitions from argon have also been observed in LHD in the visible range. The wavelengths of the VUV lines suitable for the plasma diagnostics are summarized in Table 4, showing the availability of the CIII-V, NeIII-IX, ArIII-VIII and ArXV-XVI lines.

Finally, we should notice on uncertainties of the signal relative intensities in the tables. Many discharges (≥ 100 shots) were required in order to record the VUV spectra scanning the wavelength. However, it is impossible to produce the identical discharge in all discharges, i.e., T_e and n_e, due to changes of NBI input power and wall conditioning. The influx of externally applied gas puff such as Ne and Ar is a function of edge electron temperature. Furthermore, the helical plasma has free boundary whereas the tokamak plasma has a fixed boundary. Thus, the edge plasma parameters are easily changed with a variety of the density and input heating power. The VUV emissions reported here are located in the plasma edge region and the intensities become much sensitive to the edge plasma condition. The relative intensities indicated in the table should be used only as a reference for experimentalist.
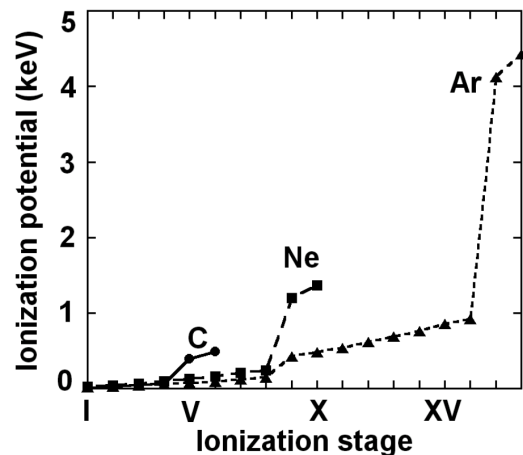

Fig. 3 Ionization potential of carbon, neon and argon ions as a function of ionization stages.

3.2 Ion temperature from Doppler broadening

Ionization potential (IP) increases when the ionization stage of impurity ions rises or the nuclear number Z of impurity elements increases, as shown in Fig. 3. The IP gradually increases with the ionization stages except for He- and H-like ions. The impurities in such ionization stages usually locate in some radial position of the plasma when the central electron temperature is high enough as compared to the IPs. In contrast, the IP of He-like ions becomes very high, since the ionization of the 1s electron requires a large energy compared with the ionization of $n = 2$ elec-
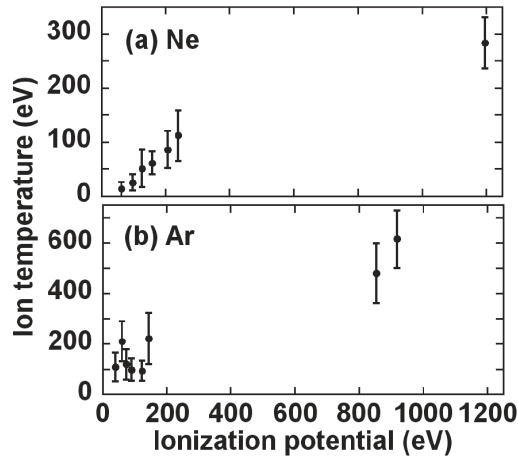
Fig. 4   Ion temperature evaluated from Doppler broadening of (a) neon and (b) argon VUV lines.
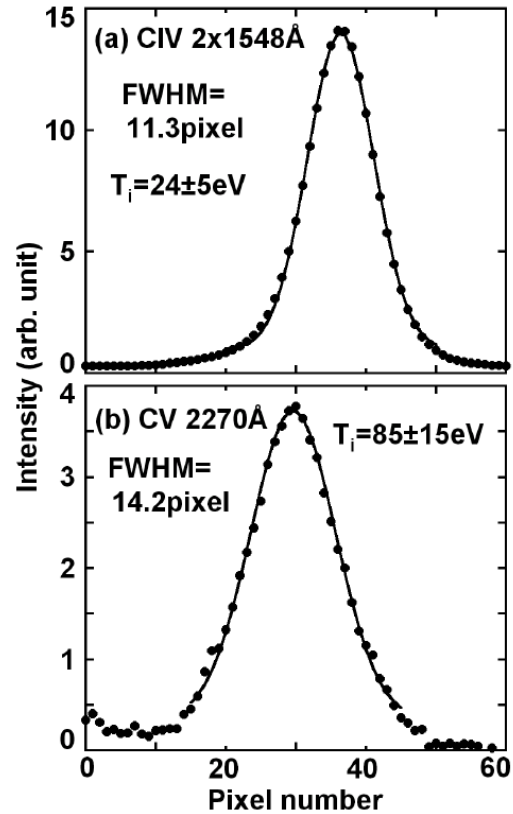

Fig. 5   Spectral profiles of (a) $2 \times$ CIV and (b) CV with Doppler broadening. Solid circles indicate raw experimental data and solid lines are fitting curves with Gaussian profiles.

trons. Therefore, these emissions are useful for the ion temperature measurement at the plasma center.

Figure 4 shows the ion temperature evaluated from the Doppler broadening of the measured VUV line emissions of neon and argon as a function of the IPs. The ion temperature of neon ions in various ionization stages is distributed in a range of 1/2-1/4 of the ionization potential in each ion. However, the ion temperature of argon ions is closely distributed to the IP. This is based on the difference in the central ion temperature. It is well known that high ion temperature operation is possible for the rare gas discharges in LHD [32, 33]. The central ion temperature of neon discharges ranges between 3-5 keV. In case of the argon discharges, the ion temperature further increases up to 10-13 keV mainly due to the lower ion density, which leads to the increase in the ion heating power density.

The measurement of ion temperature is also useful for the identification of unclassified Ar lines. Several unclassified Ar lines appear in Table 3. We also measured the ion temperature from the unclassified Ar lines. The ionization stages of such unclassified Ar lines can be estimated from Fig. 4 (b) using the measured ion temperature. Thus, the unclassified Ar lines of 486.60 Å, 618.63 Å and 619.04 Å are identified with their possible ionization stages. The results are indicated in the brackets after 'ArUn'.

3.3   Line profile analysis of absorption spectra

The line profile of the Doppler broadening has a Gaussian shape if it is assumed that the atoms or ions have a Maxwellian velocity distribution as follows:

$$I(\lambda) = \frac{1}{\sqrt{\pi}\Delta_D} \exp\left(-\frac{(\lambda - \lambda_0)^2}{\Delta_D^2}\right), \qquad (1)$$

where λ_0 is the center wavelength in Å and Δ_D the Doppler width. The Doppler width at full width at half maximum

(FWHM), Δ_{FWHM}, is given by

$$\Delta_{FWHM} = 2\sqrt{\ln 2}\Delta_D$$
$$= 7.71 \times 10^{-5} \lambda_0 \sqrt{\frac{T_i}{M}}. \qquad (2)$$

The ion temperature in eV is thus given by

$$T_i = 1.68 \times 10^8 M (\Delta_{FWHM}/\lambda_0)^2, \qquad (3)$$

where M is the atomic weight. Measured spectral lines are fitted by the Gaussian profile of Eq. (1) and the ion temperature is obtained using Eq. (3). Typical examples of the results are shown in Fig. 5 for the CIV 2×1548 Å and CV 2270 Å lines. The experimental data can be fitted by the Gaussian profile. The ion temperature obtained from this fitting is indicated in the figure.

On the other hand, neutral lines, especially Lyman-series lines (1s-np, $n \geq 2$) excited from hydrogen neutrals, have a line profile completely different from the Doppler profile. This is found in relatively high-density ($> 3.0 \times 10^{19}$ m^{-3}) discharges of LHD. Typical results on Lyman-α (HI: 1s-2p) are shown in Fig. 6. Experimentally measured line profiles are denoted with solid circles. The Lyman-α lines are measured at the second order emission (2×1215.67 Å) in order to increase the spectral resolution. It is clearly seen that the top of the profile is deformed with
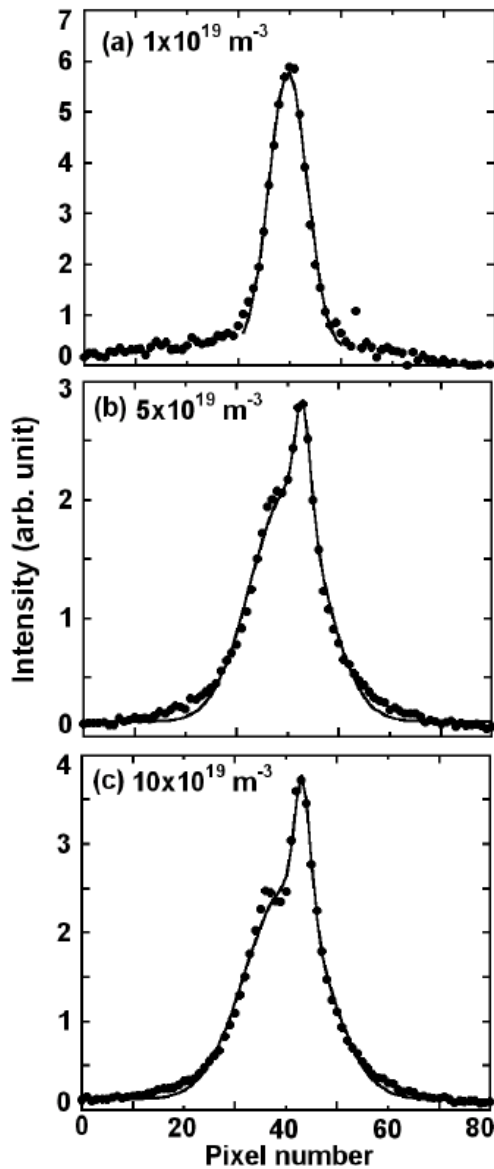
Fig. 7 Line profile of hydrogen Lyman-β (2×1025.72 Å) with self-absorption. Solid circles indicate raw experimental data in line-averaged electron density of $\overline{n_e} = 10 \times 10^{19}$ m^{-3}. Solid line is self-absorption fitting curve with $T_i = 2.4 \pm 1.2$ eV ($\Delta_D = 5.1$ pixels) and $T_n = 2.0 \pm 0.5$ eV ($\Delta_{SA} = 2.1$ pixels).

Fig. 6 Line profiles of hydrogen Lyman-α (2×1215.67 Å) with self-absorption. Solid circles indicate raw experimental data in line-averaged electron density of (a) $\overline{n_e} = 1 \times 10^{19}$ m^{-3}, (b) $\overline{n_e} = 5 \times 10^{19}$ m^{-3} and (c) and $\overline{n_e} = 10 \times 10^{19}$ m^{-3}. Solid lines express (a) Gaussian fitting curve with $T_i = 1.5 \pm 0.5$ eV ($\Delta_D = 5.2$ pixels) and self-absorption fitting curves with (b) $T_i = 9.2 \pm 1.0$ eV ($\Delta_D = 10.2$ pixels), $T_n = 0.5 \pm 0.2$ eV, ($\Delta_{SA} = 2.1$ pixels) and (c) $T_i = 11.4 \pm 1.1$ eV ($\Delta_D = 11.2$ pixels), $T_n = 0.5 \pm 0.2$ eV ($\Delta_{SA} = 2.2$ pixels).

electron density. It is well known that the neutral line is absorbed by the background neutral atoms [34].

　　The self-absorption line profile [35] is expressed using the Doppler broadening line profile as follows:

$$I_{SA}(\lambda) = I(\lambda) \exp(-kl). \qquad (4)$$

The atomic absorption coefficient k is given by

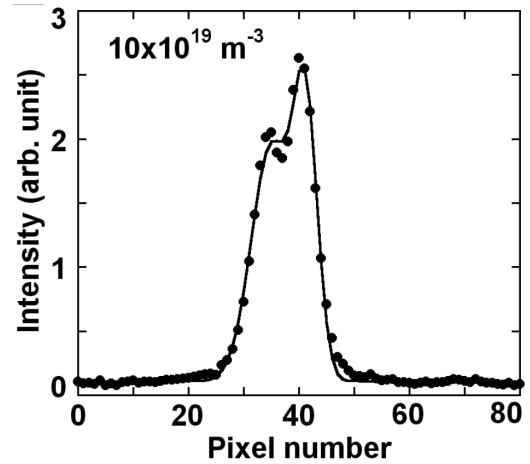$$k = k_0 \exp\left(-\frac{(\lambda - \lambda_0)^2}{\Delta_{SA}^2}\right), \qquad (5)$$

where k_0 is the atomic absorption coefficient at the center of the line and l the path length of absorption. The self-absorption line profile is then given by

$$I_{SA}(\lambda) = \frac{1}{\sqrt{\pi}\Delta_D} \exp\left(-\frac{(\lambda - \lambda_0)^2}{\Delta_D^2}\right)$$
$$\times \exp\left\{-k_0 l \exp\left(-\frac{(\lambda - \lambda_{SA})^2}{\Delta_{SA}^2}\right)\right\}. \qquad (6)$$

Taking the 0-th and 1st order terms after the expansion of Eq. (6), Eq. (6) is replaced by the following equation:

$$I_{SA}(\lambda) = \frac{1}{\sqrt{\pi}\Delta_D} \exp\left(-\frac{(\lambda - \lambda_0)^2}{\Delta_D^2}\right)$$
$$\times \left\{1 - k_0 l \exp\left(-\frac{(\lambda - \lambda_{SA})^2}{\Delta_{SA}^2}\right)\right\}, \qquad (7)$$

where $k_0 l$ is the optical depth, λ_{SA} the center wavelength of absorption and Δ_{SA} the absorption width. The self-absorption spectra of the Lyman-α line shown in Fig. 6 are fitted by the Eq. (6), which is expressed by a solid line. The measured Lyman-α line profile is in close agreement with consideration of the self-absorption process. Here, the value of T_i defines the temperature of the neutral hydrogen emitting Lyman-α and -β and the value of T_n defines the temperature of the background hydrogen absorbing the Lyman-α and -β emissions are different. This indicates that the hydrogen atoms as emitters and absorbers stay in different temperature regions. The self-absorption is also shown in Fig. 7 for the Lyman-β line (2×1025.72 Å). The line profile of Lyman-β is a very similar to that of Lyman-α and can be well explained by the absorption process. Since the intensity of Lyman-β is considerably weaker than that of Lyman-α, the line profile of Lyman-β emitted in the recombination phase at the end of discharges is used to obtain brighter intensity. In this case, then, it is expected

that the radiators and absorbers exist in similar temperature regions. The difference between λ_0 and λ_{SA} indicates a relative difference in flow velocity between radiators and absorbers. The values of difference in Fig. 6 (c), 6 (b) and Fig. 7 are 0.24 Å, 0.26 Å and 0.96 Å, respectively.

This absorption process is of course a function of edge neutral density n_n and the length of the neutral atoms l. The product of neutral number density and length of neutral atoms, $n_n l$, is given by $k_o l$ in Eq. (6) and T_n in eV as follows:

$$n_n l = 1.67 \times 10^{15} k_o l \sqrt{1.67 \times 10^4 T_n} . \tag{8}$$

The optical depth of $k_o l$ can be obtained from line fitting by Eq. (7), as shown in Fig. 6 and is determined to be $k_o l = 0.55$ at $\overline{n_e} = 5 \times 10^{19} \, \mathrm{m}^{-3}$ and $k_o l = 0.70$ at $\overline{n_e} \sim 10 \times 10^{19} \, \mathrm{m}^{-3}$. The T_n is derived from Δ_{SA} with Eqs. (2) and (3). The instrumental width of the spectrometer for Δ_{SA} is neglected in this analysis. The value of the optical depth is now insensitive to the density variation. When $T_n = 0.5 \, \mathrm{eV}$ and $k_0 l = 0.55$ at $\overline{n_e} = 5 \times 10^{19} \, \mathrm{m}^{-3}$ is assumed as seen in Fig. 6 (b), we obtain $n_n l = 7.0 \times 10^{16} \, \mathrm{m}^{-2}$ using Eq. (8). Finally, we obtain the length of the neutral hydrogen of $l = 10 \, \mathrm{cm}$ (1 cm) at $n_n = 7.0 \times 10^{17} \, \mathrm{m}^{-3}$ ($7.0 \times 10^{18} \, \mathrm{m}^{-3}$). This is fairly reasonable taking into account the measurement of neutral density obtained from visible spectroscopy where the only $n_n l$ is obtained [36]. Therefore, this result suggests that hydrogen emissions are absorbed at the plasma edge region.

4. Summary

High-resolution spectra (250 to 2300 Å) have been measured in a wavelength range of 250 Å to 2300 Å using a 3 m normal incidence spectrometer in LHD and spectra from C, Ne and Ar have been recorded with a sufficient signal-to-noise ratio. The line identification, the relative intensity and the Doppler temperature of the VUV lines are analyzed. Wavelengths of the measured VUV lines in several ionization stages (CIII-V, NeIII-IX, ArIII-VIII and ArXV-XVI) are accurately determined and tabulated including not only the E1 lines but also the M1 lines for alternative passive spectroscopy. The self-absorption of VUV lines are found for hydrogen Lyman-series lines in high-density LHD discharges. These lines are analyzed using the absorption equation. The spectroscopic data reported here are applicable to high-temperature plasma diagnostics.

[1] W.-Ü L. Tchang-Brillet and V.I. Azarov, Phys. Scr. T**100**, 104 (2002).
[2] R.C. Isler, Fusion Eng. Des. **34-35**, 115 (1997).
[3] W. Biel *et al.*, Fusion Sci. Technol. **47**, 246 (2005).
[4] K. Ebisawa *et al.*, Rev. Sci. Instrum. **70**, 328 (1999).
[5] V.A. Soukhanovskii *et al.*, Rev. Sci. Instrum. **72**, 3270 (2001).
[6] R. Barnsley *et al.*, Rev. Sci. Instrum. **74**, 1969 (2003).
[7] H. Kubo *et al.*, Nucl. Fusion **33**, 1427 (1993).
[8] D.G. Nilson, M.E. Fenstermacher and R. Ellis, Rev. Sci. Instrum. **70**, 738 (1999).
[9] J. Miyazawa *et al.*, Fusion Eng. Des. **34-35**, 235 (1997).
[10] T. Sugie *et al.*, JAERI-M 93-057 (1993).
[11] Y. Okamoto *et al.*, Rev. Sci. Instrum. **72**, 4366 (2001).
[12] M.J. May *et al.*, Phys. Rev. E **61**, 3042 (2000).
[13] S. Morita and M. Goto, Rev. Sci. Instrum. **74**, 2036 (2003).
[14] R. Katai, S. Morita and M. Goto, Rev. Sci. Instrum. **77**, 10F307 (2006).
[15] H.P. Garnir and P.H. Lefèbvre, Nucl. Instrum. Methods Phys. Res. B **235**, 530 (2005).
[16] M.F. Stamp *et al.*, CRPP EPFL LRP 220 (1983).
[17] N.J. Peacock, M.F. Stamp and J.D. Silver, Phys. Scr. T**8**, 10 (1984).
[18] H. Kubo *et al.*, JAERI-M 88-126 (1988) [*in japanese*].
[19] A.J.J. Raassen *et al.*, Astron. Astrophys. Suppl. Ser. **95**, 223 (1992).
[20] A.G. Trigueiros *et al.*, J. Opt. Soc. Am. B **14**, 2463 (1997).
[21] I. Lesteven-Vaïsse *et al.*, Phys. Scr. **38**, 45 (1988).
[22] P.S. Antsiferov *et al.*, Phys. Scr. **62**, 127 (2000).
[23] R.L. Kelly, J. Phys. Chem. Ref. Data. **16**, Suppl. 1 (1987).
[24] D.A. Verner, E.M. Verner and G.J. Ferland, At. Data Nucl. Data Tables **64**, 1 (1996).
[25] B. Denne and E. Hinnov, J. Opt. Soc. Am. B **1**, 699 (1984).
[26] C. Breton *et al.*, J. Phys. E: Sci. Instrum. **20**, 554 (1987).
[27] J.Z. Klose and W.L. Wiese, J. Quant. Spectrosc. Radiat. Tansfer. **42**, 337 (1989).
[28] M. Mimura *et al.*, Jpn. J. Appl. Phys. **29**, 2831 (1990).
[29] V. Kaufman and J. Suger, J. Phys. Chem. Ref. Data. **15**, 321 (1986).
[30] R. Katai, S. Morita and M. Goto, J. Plasma Fusion Res. Ser. **7**, 9 (2006).
[31] R. Katai, S. Morita and M. Goto, J. Quant. Spectrosc. Radiat. Transfer **107**, 120 (2007).
[32] S. Morita, M. Goto, Y. Takeiri *et al.*, Nucl. Fusion **43**, 899 (2003).
[33] Y. Takeiri, S. Morita *et al.*, Nucl. Fusion **45**, 565 (2005).
[34] R.C. Isler *et al.*, Phys. Plasma **4**, 355 (1997).
[35] J. Laimer *et al.*, Meas. Sci. Technol. **6**, 1413 (1995).
[36] M. Goto and S. Morita, Phys. Rev. E **65**, 026401 (2002).